Thermodynamic properties of ammonia clusters $(NH_3)_n$ $n=2-11$: Comparing classical and quantum simulation results for hydrogen bonded species

C. Lubombo,[1] E. Curotto,[1,a)] Paula E. Janeiro Barral,[2] and Massimo Mella[2,b)]
[1]*Department of Chemistry and Physics, Arcadia University, Glenside, Pennsylvania 019038-3295, USA*
[2]*School of Chemistry, Cardiff University, Cardiff CF10 3AT, United Kingdom*

(Received 14 October 2008; accepted 29 May 2009; published online 21 July 2009)

Classical and quantum simulations of ammonia clusters in the dimer through the hendecamer range are performed using the stereographic projection path integral. Employing the most recent polarizable potential to describe intermolecular interactions, energetic and structural data obtained with our simulations provide support for a more fluxional or flexible nature at low temperature of the ammonia dimer, pentamer, and hexamer than in the other investigated species. The octamer and the hendecamer display a relatively strong melting peak in the classical heat capacity and a less intense but significant melting peak in the quantum heat capacity. The latter are shifted to lower temperature (roughly 15 and 40 K lower, respectively) by the quantum effects. The features present in both classical and quantum constant volume heat capacity are interpreted as an indication of melting even in the octamer case, where a large energy gap is present between its global minimum and second most stable species. We develop a first order finite difference algorithm to integrate the geodesic equations in the inertia ellipsoid generated by n rigid nonlinear bodies mapped with stereographic projections. We use the technique to optimize configurations and to explore the potential surface of the hendecamer. © *2009 American Institute of Physics*.
[DOI: 10.1063/1.3159398]

I. INTRODUCTION

Ammonia and ammonia clusters are a source of data fundamental to many applied science and engineering fields, such as geology,[1] atmospheric chemistry,[2] and energy storage research,[3] to name a few examples. The dominant interaction responsible for the cohesion of ammonia molecules into clusters is the hydrogen bond. However, ammonia is unlike other textbook examples of hydrogen bonded species, since each ammonia molecule has the potential to coordinate with three other molecules. In the bulk crystal, in fact, each molecule is a triple acceptor as well as a triple donor.[4] As such, homogeneous ammonia clusters constitute an important variation on the directional nature of the hydrogen bond. Consequently, ammonia clusters have been the focus of intense experimental[5–12] and theoretical[13–19] investigations for nearly three decades. The main focus of the investigations has been the elucidation of their structures using primarily scattering, microwave, and infrared spectroscopy experiments. The bulk of the early work focused on the dimer and the systematic development of a hierarchy of potential energy models that reproduce spectroscopic properties of small clusters[20–22] on one hand and condensed phase data[23–26] on the other. More recent investigations have focused on the vibrational spectra of small to midsized ammonia clusters.[17,19] Some intramolecular bands are particularly sensitive to clustering and the coordination number on the ammonia molecule. Ammonia clusters have been grown in helium droplets[10] at 0.38 K, and their infrared spectra confirm that as few as 1000 molecules are sufficient to produce a structure of the inner molecules similar to the crystal structure of the bulk. Argon clusters, on the other hand, have been shown to begin transitioning at the core from the icosahedral to the bulk cuboctahedral fcc arrangements only after the 14th solvation layer is completed,[27] requiring well over 10^4 atoms.

Motivated by an analysis of the performance for literature ammonia pair potentials,[28] in recent work, we have developed an analytical model for the potential energy surface (PES) of ammonia clusters which includes many-body contributions, by the addition of a noniterative charge on a spring (COS) computation of the induction terms.[29] The parameters of the model were obtained by fitting *ab initio* data. The structures of the global minima of $(NH_3)_n$ $(n=3-20)$ were found to be in agreement with those obtained by additive potentials, with the exception of the pentamer, for which we have reported a new low energy isomer. The binding energy is larger for all sizes when compared with that obtained by additive potentials. The clusters investigated in Refs. 28 and 29 show distinct patterns in the energy difference from the global minimum of the lowest 200 isomers. After inspecting the energy difference from the global minimum of the most important configurations of the PES and observing how the pattern changes as a function of size, it is only natural to speculate about how the thermodynamic behavior may differ from one size to the next. However, with one exception,[13] no thermodynamic investigation on ammo-

a)Electronic mail: curotto@arcadia.edu.
b)Electronic mail: mellam@cardiff.ac.uk.

nia clusters has been reported. Virtually nothing is known about the classical or quantum thermodynamic behavior of midsized ammonia clusters, let alone about the possible interplay between size and quantum effects in defining the possible fluxional nature (i.e., the facile interconversion between different isomers) for these species. Two decades ago, Marchi *et al.* performed path integral simulations of $(NH_3)_n$, $n=16$, 36, and 54 at 100 and 200 K, in connection with the electron attachment problem.[13] Since that time, the community has developed a number of tools that improve substantially the efficiency of classical and path integral[30–56] Monte Carlo simulations. It is now possible to accelerate the convergence of the Cartesian path integral without the need to evaluate derivatives of the PES, for example.[50–56]

In order to simulate aggregated molecular matter with path integrals, other developments proved important. At the temperatures where molecular clusters are thermodynamically stable, the intramolecular degrees of freedom are predominantly in the ground state and converging path integral simulations with flexible molecules are prohibitive even for dimers. On the other hand, the path integral simulation of cluster (or liquids) composed of rigid bodies is not simple. Kuharski and Rossky simulated liquid water with angular variables using the body fixed frame and neglecting precessions.[46] The resulting path integral is numerically convergent to the exact result but only to first order and only the discretized version of the path integral can be applied. The precessions of the asymmetric tops contribute second order terms in the density matrix. Therefore, using the gradient of the potential to accelerate the convergence of path integrals will not work in the body fixed frame. For these reasons, there are only few path integral simulations of molecular matter in the literature.[35–41,43–49] Using stereographic projection coordinates, we have been able to develop a map for rigid tops that allows us to perform path integral simulations using the space fixed frame and the reweighted random series approach.[35–40,45] The energy and heat capacity estimators based on finite differences[54] were shown to retain the cubic convergence property in the curved spaces mapped stereographically in conjunction with the reweighted random series method.[39]

The purpose of this article is to report the results of our investigation on ammonia clusters in the dimer through the hendecamer range. With our newly developed potential energy model[29] and the numerical methods available at our disposal, we formulate the following objectives. The evaporation energy of the clusters in Ref. 28 suggested the possible presence of high stability for a particular size, a so-called magic number. The presence of magic numbers is usually associated with the completion of a shell with a particular symmetry, which normally optimizes the balance between the surface tension and the details of the repulsive interactions. However, molecular motion may influence the relative stability of different cluster sizes, and in the present investigation we seek to determine the importance of the effects of temperature and the effects of quantum fluctuations on the binding energy of the ammonia clusters $(NH_3)_n$ in the $n=2-11$ range, as well as the possible presence of multiple isomers at low temperatures. This quantity allows one to assess the possible appearance of magic number clusters, as it has recently been shown by means of statistical simulations.[57] At the same time, we seek to determine patterns in the classical and quantum heat capacity of the systems. Specifically, we seek to determine the evaporation temperature range and to determine whether the clusters melt in the classical and in the quantum limit. In this respect, it is instructive to characterize thermodynamic behaviors extracted from simulations in terms of the structural properties of the most favorable configurations and other popular structural indicators based on the collective fluctuations of classes of degrees of freedom. We additionally seek to establish the strength of the correlations between the intermolecular radial degrees of freedom and the relative orientations of the molecules and to determine how these are affected by temperature and quantum fluctuations.

We organize the rest of this article in the following way. The details of the PES are reproduced in Sec. II A for the reader's convenience.[29] In Sec. II B, we provide the details of how the ellipsoid of inertia space for n rigid bodies can be mapped stereographically. Section II C contains details of the stereographic projection path integral approach. In Sec. II D, we develop a point slope molecular dynamics algorithm that uses finite difference for the integration of Newtonian and Brownian dynamics in manifolds. The algorithm avoids the need to compute directly the numerous connection coefficients that appear in the geodesic equations. The method is developed to find the important minima and to explore further the PES for the hendecamer, which proves to be a particularly challenging system to simulate. In Sec. II E, we describe the methods used to characterize the classical and quantum random walks. The results of the classical and quantum simulations and their structural analysis are reported in Secs. III A and III B, respectively. Section IV contains our discussions and conclusions.

II. METHODS

A. The potential energy model

The potential energy model for the ammonia clusters has been developed in a recent investigation by fitting *ab initio* data obtained using second order Møller–Plesset perturbation theory. The *ab initio* treatment includes extended basis sets and basis set superposition error corrections with the counterpoise procedure. In the same work, the *ab initio* data set is fitted to an analytical function.[29] The potential energy contains the following terms:

$$V(\mathbf{r}) = V_{\mathrm{Coul}} + V_{\mathrm{rep}} + V_{\mathrm{disp}} + V_{\mathrm{ind}} + V_C. \quad (1)$$

The V_{Coul}, V_{rep}, V_{disp}, and V_{ind} terms are the constituents of the model optimized in Ref. 29, with the model $C(\mathrm{pol}, Q^{\mathrm{opt}})$ parametrization. V_{Coul} is the Coulombic interaction resulting between pairs of charged centers located in separate ammonia molecules. A charge of +0.5264 a.u. is located on each of the hydrogen nuclei, and a charge of −1.5792 a.u. is located 0.295 bohr away from the nitrogen nucleus, toward the hydrogens along the C_3 axis of symmetry.[22]

V_{rep} is the repulsion term computed as a sum of repulsive interactions between pairs of atoms located on separate ammonia molecules,

$$V_{rep} = \sum_{j>i} a_{ij} \exp[-b_{ij}(r_{ij} - r_{ij}^*)]. \quad (2)$$

The dispersion term is computed as a function of the nitrogen-nitrogen distance between pairs of ammonia molecules,

$$V_{disp} = -\sum_{i,j>i}^{n} f(r_{N_iN_j})\left(\frac{d_6}{r_{N_iN_j}^6} + \frac{d_8}{r_{N_iN_j}^8} + \frac{d_{10}}{r_{N_iN_j}^{10}}\right), \quad (3)$$

where $f(r_{N_iN_j})$ is a smooth switch,

$$f(r_{N_iN_j}) = \begin{cases} 1, & r_{N_i,N_j} > r^*, \\ \exp\left[-\dfrac{(r_{N_iN_j} - r^*)^2}{r_{N_iN_j}^2}\right], & r_{N_iN_j} < r^*, \end{cases} \quad (4)$$

and $r^* = 8.882$ bohrs.

The V_{ind} term is a single-step COS representation of the induction, where a fixed charge of $q=16$ a.u. is placed at $\mathbf{r}_0$, i.e., on the nitrogen atom, and the moving charge equal in magnitude is displaced from the fixed charge using

$$\mathbf{r}_m = \mathbf{r}_0 - \alpha_{MP2}\mathbf{F}/q, \quad (5)$$

where $\alpha_{MP2} = 14.19$ bohrs^3 is the spherically averaged molecular polarizability and $\mathbf{F}$ the external electric field. The induction energy is computed using the following sum over all the ammonia molecules:

$$V_{ind} = -\sum_{i=1}^{n} S(r)\left(\frac{1}{2}\mu_i^{(0)} \cdot \mathbf{E}_i^{(0)} + \frac{1}{2}\mu_i^{(0)} \cdot \mathbf{E}_i^{(1)}\right), \quad (6)$$

where $\mu_i^{(0)}$ is the dipole induced in the ith molecule by the initial external electric field felt by the ith molecule, $\mathbf{E}_i^{(0)}$, resulting from the fixed charges of the $n-1$ ammonia molecules surrounding it. $\mathbf{E}_i^{(1)}$ is the total external electric field felt by the ith molecule after the displacement of the induction charge q according to Eq. (5) with $\mathbf{F}_j = \mathbf{E}_j^{(0)}$ for all the ammonia molecules has been computed. The noniterative procedure is found to provide more than 95% of the self-consistent estimate of the induction energy in ammonia clusters.[29] By using only a single step in the COS recursion the analytical model accounts for inductions in an efficient and convenient way, since the resulting analytical expression is a smooth function. The function $S(r)$ in Eq. (6) is a smooth switch,

$$S(r) = \tfrac{1}{2}\{1 + \tanh[10(r-1)]\}, \quad (7)$$

where r is the distance between any atom in molecule j and the nitrogen atom of molecule i. $S(r)$ turns off the induction interactions when a hydrogen atom is too close to the nitrogen of another ammonia molecule.

Lastly, in Eq. (1), V_C is the Lee–Barker–Abraham smooth reflecting sphere, required to define the volume occupied by the cluster,

TABLE I. Parameters for the model $C(\text{pol}, Q^{\text{opt}})$ (Ref. 29).

Parameter symbol	Value	Units
a_{NN}	14.602 1	hartree
b_{NN}	1.394 38	bohr^{-1}
r_{NN}^*	0.00	bohr
a_{NH}	$6.816\,05 \times 10^{-4}$	hartree
b_{NH}	1.905 62	bohr^{-1}
r_{NH}^*	4.925 68	bohr
a_{HH}	1.115 52	hartree
b_{HH}	1.957 96	bohr^{-1}
r_{HH}^*	0.00	bohr
r^*	8.882	bohr
d_6	98.264 5	hartree bohr^6
d_8	1 684.55	hartree bohr^8
d_{10}	38 962.98	hartree bohr^{10}

$$V_C = \sum_{i=1}^{n}\left(\frac{\mathbf{r}_{N_i} - \mathbf{R}_{CM}}{2R_C}\right)^{20}, \quad (8)$$

where $\mathbf{r}_{N_i}$ is the location of the nitrogen atom for the ith ammonia molecule, $\mathbf{R}_{CM}$ is the center of mass of the cluster, and R_C is 9.0 bohrs. The optimized values of the parameters a_{ij}, b_{ij}, r_{ij}^*, d, d_6, d_8, and d_{10} are reproduced in Table I in a.u.

B. The ellipsoid of inertia space for *n* rigid bodies and its map

For a given configuration of n ammonia molecules, we introduce a set of coordinates q^μ, $\mu = 1, \ldots, 6n$, where for the ammonia molecule j, $q^{6(j-1)+1}$, $q^{6(j-1)+2}$, and $q^{6(j-1)+3}$ are the Cartesian coordinates of the center of mass of the molecule and $q^{6(j-1)+4}$, $q^{6(j-1)+5}$ and q^{6j} are the three stereographic projection coordinates used to map the orientation of the rigid molecule.[35–39] In Ref. 36 we develop the stereographic projection coordinates map for inertia ellipsoids $\mathbb{I}$. The change of coordinates is obtained starting with the four quaternion parameters as functions of the three Eulerian angles,[46]

$$x^1 = \cos\frac{\theta}{2}\cos\left(\frac{\psi+\phi}{2}\right), \quad (9a)$$

$$x^2 = \sin\frac{\theta}{2}\cos\left(\frac{\psi-\phi}{2}\right), \quad (9b)$$

$$x^3 = \sin\frac{\theta}{2}\sin\left(\frac{\psi-\phi}{2}\right), \quad (9c)$$

$$x^4 = \cos\frac{\theta}{2}\sin\left(\frac{\psi+\phi}{2}\right). \quad (9d)$$

The quaternion parameters in Eq. (9) satisfy a spherical-like constraint relation,

$$(x^1)^2 + (x^2)^2 + (x^3)^2 + (x^4)^2 = 1. \quad (10)$$

Therefore, the rotation space expressed in term of quaternions is a 3-sphere, $\mathbb{S}^3$. A general map from hyperspheres of dimension d to stereographic projections is formulated as follows.[36] The set of generalized stereographic projections is

a set of d independent coordinates $\{\xi^{\mu}\}_{\mu=1}^{d}$ defined by

$$\frac{x^i}{1-x^{d+1}} = \frac{\xi^i}{2}, \quad i = 1,2,\ldots,d. \tag{11}$$

The fundamental object of interest is the Hessian metric tensor,[58] which is obtained by the transformation law of 2-forms,

$$g_{\mu\nu} = \frac{\partial q^{\mu'}}{\partial \xi^{\mu}} \frac{\partial q^{\nu'}}{\partial \xi^{\nu}} g_{\mu'\nu'}. \tag{12}$$

If $\mathbb{I}$ is mapped with Euler angles, $q^1=\theta$, $q^2=\phi$ and $q^3=\psi$, then $g_{\mu'\nu'}$ is represented by the following symmetric matrix:

$$g_{11} = I_{xx}\cos^2\psi + I_{yy}\sin^2\psi, \tag{13a}$$

$$g_{12} = (I_{xx} - I_{yy})\sin\theta\sin\psi\cos\psi, \tag{13b}$$

$$g_{13} = 0, \tag{13c}$$

$$g_{22} = I_{xx}\sin^2\theta\sin^2\psi + I_{yy}\sin^2\theta\cos^2\psi + I_{zz}\cos^2\theta, \tag{13d}$$

$$g_{23} = I_{zz}\cos\theta, \tag{13e}$$

$$g_{33} = I_{zz}, \tag{13f}$$

where I_{xx}, I_{yy}, and I_{zz} are the elements of the inertia tensor in the body fixed frame. For n rigid bodies mapped with the set of coordinates q^{μ}, $\mu=1,\ldots,6n$, the metric tensor takes the following block diagonal form:

$$g_{\mu\nu} = \mathrm{diag}\{g_{\mu\nu}^{(1)}, g_{\mu\nu}^{(2)}, \ldots, g_{\mu\nu}^{(n)}\}, \tag{14}$$

where $g_{\mu\nu}^{(j)}$ is the metric tensor block associated with the jth rigid top and it is represented by a 6×6 symmetric matrix,

$$g_{\mu\nu}^{(j)} = \begin{pmatrix} m_j & 0 & 0 & \mathbf{0} \\ 0 & m_j & 0 & \mathbf{0} \\ 0 & 0 & m_j & \mathbf{0} \\ \mathbf{0} & \mathbf{0} & \mathbf{0} & g_{\mu\nu}^{\mathbb{I},(j)} \end{pmatrix}. \tag{15}$$

In Eq. (15), the symbol **0** represents 3 rows if above the main diagonal, and 3 columns if below, with all zero entries, m_j is the total mass of the jth top, and $g_{\mu\nu}^{\mathbb{I},(j)}$ is the metric tensor for the ellipsoid of inertia computed using Eq. (12). The primed version of the metric tensor $g_{\mu'\nu'}$ in Eq. (12) is in Eq. (13). The partial derivatives in Eq. (12) are obtained[36] from Eq. (11).

C. Stereographic projection path integral

Path integration[30] in manifolds was first considered in the late 1950s by DeWitt.[31] DeWitt was the first to demonstrate that the Feynman path integral can be evaluated, in principle, in coordinate systems other than Cartesian. In manifolds, the choice of coordinates is often crucial. The general rule seems to dictate that a coordinate set defined to map points from the manifold to its universal covering space simplifies the numerical task. For example, Schulman evaluated the partition function for the free particle in a ring analytically[32] using a map for $\mathbb{S}^1\to\mathbb{R}^1$. The stereographic projection coordinates we use in the present work are defined by a map with the same mathematical property. The path integral in manifolds is important in high energy physics and in quantum field theory,[33] and it is possible to formulate path integrals over continuous groups, subgroups, and spaces with curvature and torsion.[22,34] Despite of all these successes, only a handful of stochastic path integral computations with holonomic constraints are found in the literature.[46–49] Stochastic path integration in manifolds is particularly difficult if angles are used as coordinates. For example, it is not possible to expand paths using random series in manifolds that are mapped with open sets. This problem is eliminated with the use of stereographic projections, since the range of stereographic projection coordinates extends from $-\infty$ to $+\infty$. The ability to expand the Brownian bridge in terms of random series makes it possible to derive the Feynman–Kac equivalent in manifolds.[35] In turn, the Feynman–Kac equivalent in manifolds allows us to formulate higher order convergence using partial averaging[37] and reweighted random series methods for stereographic projection path integrals.[38,39] In our recent simulation of water clusters, we refine the algorithm for the Fourier–Wiener reweighted random series expansion, show that it is possible to formulate the efficient finite difference estimators for the energy and heat capacity, and provide some details of the proof that their convergence is cubic as it is in Euclidean spaces.[50–56]

In manifolds, the expression for the density matrix is

$$\rho(q,q',\beta) = \left(\frac{1}{2\pi}\right)^{ND/2} (\hbar^2\beta)^{-D/2} J_{\Lambda} \times \int d[a]_r \exp\left\{-\beta\int_0^1 du U(\tilde{q}^{\mu}(u))\right\}, \tag{16}$$

where J_{Λ} is a constant Jacobian[39] and the action is

$$U(\tilde{q}^{\mu}(u)) = -\frac{N}{2\beta}\ln[\det g_{\mu\nu}(\tilde{q}^{\mu}(u))] + \frac{1}{2}g_{\mu\nu}(\tilde{q}^{\mu}(u))\dot{q}^{\mu}\dot{q}^{\nu} + V(\tilde{q}^{\mu}(u)). \tag{17}$$

$\tilde{q}^{\mu}$ is the closed path $[\tilde{q}^{\mu}(0)=\tilde{q}^{\mu}(1)]$ in the manifold with $u=\tau/\beta\hbar$. When the random series expansion is used with k_m core terms and $k_m'-k_m$ tail terms we write

$$\tilde{q}^{\mu}(u) = q_r^{\mu}(0) + \hbar\beta^{1/2}\sum_{k=1}^{k_m} a_k^{\mu}\Lambda_k(u) + \hbar\beta^{1/2}\sum_{k=k_m+1}^{k_m'} a_k^{\mu}\tilde{\Lambda}_k(u), \tag{18}$$

and we use $k_m'=4k_m$. To compute the integral in Eq. (16), we use the trapezoid rule, with $N=k_m+1$ points, and we evaluate the metric tensor and the potential at the end point of every interval $u_j=j/N$. The end point choice yields a constant curvature for the quantum Jacobian that we can ignore.[22,34] The estimators are computed using the following expressions:[39]

$$\langle E\rangle_{\beta} = \frac{D}{2\beta} + \left\langle \frac{\partial}{\partial\beta}\left[\beta\int_0^1 du U(\tilde{q}^{\mu}(u))\right]\right\rangle, \tag{19}$$

$$\frac{C_V}{k_B} = \frac{D}{2} + \frac{D^2}{4} + D\beta\left\langle \frac{\partial}{\partial\beta}\left[\beta\int_0^1 d\tau U(\tilde{q}^\mu(u))\right]\right\rangle + \beta^2\left\langle \left\{\frac{\partial}{\partial\beta}\left[\beta\int_0^1 du U(\tilde{q}^\mu(u))\right]\right\}^2\right\rangle - \beta^2\left\langle \frac{\partial^2}{\partial\beta^2}\left[\beta\int_0^1 du U(\tilde{q}^\mu(u))\right]\right\rangle - \left\{-\frac{D}{2} - \beta\left\langle \frac{\partial}{\partial\beta}\left[\beta\int_0^1 du U(\tilde{q}^\mu(u))\right]\right\rangle\right\}^2. \quad (20)$$

The derivatives with respect to β in Eqs. (19) and (20) are evaluated numerically.

Prior to performing our simulations, we carefully study the issue of excluding internal degrees of freedom, since such approximation is not generally valid and must be verified case by case. Based on the normal mode frequencies of the free ammonia molecule and on previous experience with water clusters,[39] we estimate that all the internal modes (including the lower frequency bending and the umbrella mode) are predominantly in the ground state in the range of temperatures of interest. More precisely, we estimate that the effects of thermal excitations of the internal modes of ammonia become visible on the scale of the anticipated heat capacity variation and within the statistical error in the thermodynamics only above 200 K. At these temperatures, we expect the clusters to be largely in the dissociated state. The umbrella mode has two degenerate states only in the free limit; the degeneracy is broken when other molecules are around. Therefore, the ground state wave function is dominated by one configuration instead of having an equal mixture of the two.

D. Molecular dynamics in manifolds

It is well known that the Euler–Lagrange equations,

$$\frac{d}{dt}\left(\frac{\partial\mathcal{L}}{\partial\dot{q}^\nu}\right) - \left(\frac{\partial\mathcal{L}}{\partial q^\nu}\right) = 0, \quad (21)$$

are invariant under any continuous change of coordinates,[58] and therefore are applicable in any manifold produced by holonomic constraints or any parameter space for a Lie (sub-)group of continuous transformations.[59] In manifolds, the Lagrangian takes the following general form:

$$\mathcal{L} = \tfrac{1}{2} g_{\mu\nu}\dot{q}^\mu\dot{q}^\nu - V. \quad (22)$$

V is the potential energy and $g_{\mu\nu}$ is the metric tensor. Generally, both $g_{\mu\nu}$ and V depend on the configuration q. Therefore, Eq. (21) becomes

$$g_{\mu\nu}\ddot{q}^\mu + (\partial_\nu g_{\mu\beta})\dot{q}^\mu\dot{q}^\beta - \tfrac{1}{2}(\partial_\nu g_{\mu\beta})\dot{q}^\mu\dot{q}^\beta + \partial_\nu V = 0. \quad (23)$$

The first two terms in Eq. (23) result from the time derivative of the partial of $\mathcal{L}$ with respect to $\dot{q}^\nu$. A trivial rearrangement yields the equivalent of Newton's second law in manifolds,

$$g_{\mu\nu}\ddot{q}^\mu = -\partial_\nu\mathcal{L}^+, \quad (24)$$

where $\mathcal{L}^+$ is the Lagrangian with the potential inverted,

$$\mathcal{L}^+ = \tfrac{1}{2} g_{\mu\nu}\dot{q}^\mu\dot{q}^\nu + V. \quad (25)$$

It is customary to rewrite the derivative of the metric tensor using a symmetrized version, known as the Christoffel symbols of the first kind,[58] and upon multiplication on both sides by $g^{\mu\nu}$, the inverse of the metric tensor, one derives the familiar geodesic equations for accelerated systems in manifolds.[58] For our purposes, it is more convenient to work directly with Eq. (24) since the connection coefficients[58] in ellipsoid of inertia mapped stereographically have formidable expressions. The equation we use as a starting point is obtained by multiplying by $g^{\mu\nu}$, the inverse of the metric tensor, both sides of Eq. (24). The acceleration vector becomes

$$\ddot{q}^\mu = -g^{\mu\nu}\partial_\nu\mathcal{L}^+. \quad (26)$$

The simple form of Eq. (26) suggests the following algorithm:

(1) Given the initial conditions $(q^\mu,\dot{q}^\mu)_n$ for step $n=0,1,\ldots$, compute $\partial_\nu\mathcal{L}_n^+$ by finite difference for $\nu=1,2,\ldots,d$.
(2) Compute the inverse of the metric tensor $g^{\mu\nu}$ and the product $(g^{\mu\nu}\partial_\nu\mathcal{L}^+)_n$.
(3) For sufficiently small values of Δt, assume that $(g^{\mu\nu}\partial_\nu\mathcal{L}^+)_n$ is constant, integrate, and update the velocities,

$$(\dot{q}^\mu)_{n+1} = (\dot{q}^\mu)_n - (g^{\mu\nu}\partial_\nu\mathcal{L}^+)_n\Delta t. \quad (27)$$

(4) Using a similar assumption for the velocities update the configuration,

$$(q^\mu)_{n+1} = (q^\mu)_n + (\dot{q}^\mu)_{n+1}\Delta t. \quad (28)$$

(5) Compute the energy $E(t_{n+1})=(\mathcal{L}^+)_{n+1}$, update the simulation time $t_{n+1}=t_n+\Delta t$, and repeat from step (1).

To test this algorithm, we run a 10^4 step trajectory for $(NH_3)_{11}$ with $\Delta t=50$ hartrees^{-1} (roughly 1.2 fs). The initial configuration is an unminimized cagelike hcp fragment. The starting velocities are set to zero. The energy conservation property of the algorithm is measured from the difference $E(t)-E_0$, where E_0 is the initial energy. The algorithm is surprisingly stable given that it is not symplectic and is a first order approach. The energy fluctuation $E(t)-E_0$ is a small fraction of the initial energy E_0 and appears to be constant over a relatively long simulation time. Molecular dynamics simulations in similar manifolds may require algorithms with better convergence properties. It is simple to change the present algorithm into a Verlet equivalent without any additional derivatives of the potential or the metric tensor. Additionally, we test symplectic algorithms using a general Hamiltonian formalism with finite difference of the Hamiltonian to evaluate the local split Liouville operator. We find that the resulting Candy–Rozmus algorithm (a fourth order symplectic method) is as stable as the point slope approach developed here. For the purpose of finding the closest minimum the point slope method is the most efficient. The usual dissipative term is added to Eq. (27) to produce a $T=0$ Brownian dynamics algorithm,

$$(\dot{q}^{\mu})_{n+1} = (\dot{q}^{\mu})_n - (g^{\mu\nu}\partial_{\nu}\mathcal{L}^{+})_n \Delta t - \gamma(\dot{q}^{\mu})_n \Delta t. \tag{29}$$

E. Characterization methods

We use a number of methods to examine the simulations structurally:

(i) Lindemann indices[60–69] for radii and angles.
(ii) Correlation coefficients between radial and orientation degrees of freedom.
(iii) Distributions of structural identifiers and rotationally invariant properties.
(iv) The genetic algorithm,[70–74] modified for clusters of rigid tops.
(v) The structural comparison algorithm (SCA), also modified to obtain a more favorable scaling with size.

The Lindemann index has been developed to study bond length fluctuations in molecular dynamics and Monte Carlo simulations.[60–68] The radial Lindemann index used in the present work is

$$\delta_r = \frac{2}{n(n+1)} \sum_{i<j}^{n} \frac{(\langle r_{\mathrm{N}_i\mathrm{N}_j}^2 \rangle - \langle r_{\mathrm{N}_i\mathrm{N}_j} \rangle^2)^{1/2}}{\langle r_{\mathrm{N}_i\mathrm{N}_j} \rangle}, \tag{30}$$

where n is the number of molecules of ammonia in the cluster and $r_{\mathrm{N}_i\mathrm{N}_j}$ is the size of the nitrogen-nitrogen vector between a pair of ammonia molecules. Fluctuations in the nitrogen-nitrogen "bond length" yield important information about the nature of the physical state of the system. Small values of δ_r are indicative of a solidlike state, whereas larger values indicate a liquid or a gaseous state for the cluster. Normally, sharp changes in the Lindemann index correlate with features in the heat capacity of clusters.

Each molecule of ammonia has three additional degrees of freedom, necessary to map its orientation. We find it instructive to investigate the fluctuations of the relative orientation between pairs of molecules. For each ammonia molecule, we compute the components of the unit vector along the C_3 symmetry axis. The vector along the C_3 axis is chosen to be directed from the nitrogen to the hydrogens. Letting θ_{ij} be the angle between the two vectors along the C_3 symmetry axes for molecules i and j, we define the angular Lindemann index as follows:

$$\delta_{\theta} = \frac{2}{n(n+1)} \sum_{i<j} \frac{(\langle |\theta_{ij}|^2 \rangle - \langle |\theta_{ij}| \rangle^2)^{1/2}}{\langle |\theta_{ij}| \rangle}. \tag{31}$$

The absolute value is necessary to eliminate large fluctuations produced by acceptor-donor and donor-acceptor hoppings.

A recent investigation of $(\mathrm{HCl})_n$ clusters has provided evidence that radial and angular degrees of freedom in quantum simulations of prototypical hydrogen bonded species may be strongly correlated.[40] The correlations in the HCl pentamer are strong enough to produce a quantum induced melting of the HCl pentamer. We investigate correlations between orientations and translations since they are an important part of the general dynamic features of hydrogen bonded aggregates. The correlation coefficient between the angular and radial degrees of freedom is defined as

$$\rho(\theta, r) = \frac{2}{n(n+1)} \sum_{i<j} \frac{\langle |\theta_{ij}| r_{ij} \rangle - \langle |\theta_{ij}| \rangle \langle r_{ij} \rangle}{(\langle r_{ij}^2 \rangle - \langle r_{ij} \rangle^2)^{1/2} (\langle |\theta_{ij}|^2 \rangle - \langle |\theta_{ij}| \rangle^2)^{1/2}}. \tag{32}$$

Distributions of structural identifiers[69] can be used to identify minima that are visited in the course of a random walk. Therefore, knowledge of the important minima of the PES is paramount in the interpretation of simulation results. In some cases, the distribution of structural identifiers needs to be supplemented by periodically quenching configurations, or as in the present case, a translational and rotational invariant structure comparison. The comparison between two configurations of a cluster of ammonia is carried out with the SCA,[75] which has been modified for the present work. The modifications decrease the number of necessary operations substantially. To make a comparison, we use the Cartesian coordinates of all the atoms, so the configuration A of a cluster with n rigid ammonia molecules is a set of $4n$ Cartesian vectors $\{\mathbf{r}_i^A\}_{i=1}^{4n}$, relative to the geometric center, i.e.,

$$\sum_{i=1}^{4n} \mathbf{r}_i^A = \mathbf{0}, \tag{33}$$

and oriented so that atom 1 is on the z axis and atom 2 on the x-z plane. The atoms are all treated as identical, namely, no distinction is made between H and N atoms. The algorithm to compare configurations A and B is as follows. Once the Cartesian vectors $\{\mathbf{r}_i^A\}_{i=1}^{4n}$ and $\{\mathbf{r}_i^B\}_{i=1}^{4n}$, relative to the geometric center, are known, configuration B is rotated so that atom i, $1 \le i \le 4n$, is on the z axis and atom j, $1 \le j \le 4n$, $j \ne i$, is on the x-z plane. For each of the $4n(4n-1)$ rotations, a sorting of the remaining $4n-2$ atoms is performed to find the atom of B that is the closest to atom k of A for $k=2,\ldots,4n$. Let $\Delta_{ij}^{(A)}$ represent an element of the following set of sums:

$$\Delta_{ij}^{(A)} = \sum_{k=1}^{4n} [\mathbf{r}_k^A - \mathcal{P}\mathbf{R}(\Omega_i, \Omega_j)\mathbf{r}_k^B], \tag{34}$$

where the set $\{\mathcal{P}\mathbf{R}(\Omega_i, \Omega_j)\mathbf{r}_k^B\}_{k=1}^{4n}$ is the configuration B rotated and with the labels permuted as described. The structural distance from A, denoted with the symbol $\Delta^{(A)}$, is defined as the infimum of the set,

$$\Delta^{(A)} = \inf\{\Delta_{ij}^{(A)}\}_{i,j=1, i\ne j}^{4n}. \tag{35}$$

The quantity $\Delta^{(A)}$ is most meaningful when the configuration A is a minimum of the PES. If A is the global minimum we use the symbol Δ_0.

The main departure from the original version of SCA is the use of the geometric center as the origin. In the original version, we had used atom 1 of A to define the origin. Defining atom 1 as the origin would involve $4n$ translations on top of $(4n-1)(4n-2)$ rotations. With a sorting routine that scales quadratically, the total number of operations of the original SCA would have been $4n(4n-1)(4n-2)(4n-3)^2$. In the current version it requires $4n(4n-1)(4n-2)^2$ operations. Another important difference in the application of SCA to

molecular clusters is that we have used the original version of SCA to manipulate only the Cartesian coordinates of the centers, unlike those of every atom as we do here. The measure $\Delta^{(A)}$ in the present version is sensitive to changes in the orientations of the molecules.

In our previous work we obtained the most important minima for the systems we investigate presently.[29] However, we find it necessary to rerun a minimum search for a number of sizes after finding difficulties with the parallel tempering simulations as explained in Sec. III. We use one of the operators of the genetic algorithm[70–74] to produce starting points (as "children") for the quenching algorithm. Two parent structures A and B selected using the traditional "fitness" model are translated in the center of mass and rotated by a random amount. Then, using a random number k, $1<k<n$, a child configuration is produced by using the coordinates of the first k molecules from configuration A and the remaining $n-k$ from configuration B. We use the algorithm in Sec. II D to integrate Newton's equations with a dissipative term to reach the nearest minimum. A generation consisting of 100 children is created; then each child is quenched. The new minima are sorted and compared against the pool of minima at hand so that only a single copy of each minimum is in the list of possible parents for the next generation.

III. RESULTS

A. Classical and quantum thermodynamic properties

The classical [$k_m=0$, cf. Eq. (18)] and quantum energy and heat capacity are obtained by averaging the outcome of ten independent parallel tempering[76–79] simulations. To perform a Metropolis move, first we select at random one NH_3 molecule using a random number drawn from a uniform distribution. Then, for path integral simulations, we select a particular value of k uniformly in $1\leq k\leq 4k_m$ to move the coefficients a_k^μ associated with each of the six degrees of freedom of the selected molecule. The value of the step is optimized using a simple self-adapting algorithm, the goal of which is to produce a 50% rejection for the Metropolis moves. The energy and heat capacity estimators are in Eqs. (19) and (20), respectively. In order to control the statistical quality of the results and assure reproducibility of our findings we use a 10^6 move walk to approach the asymptotic distribution, and then we use another 10^6 move walk to sample the energy and heat capacity. We repeat the procedure ten times with a different seed to obtain ten independent samples. The mean values for each block are reaveraged, and the standard error in the mean is used to compute a 95% confidence integral represented by error bars in our graphs. The standard block averaging procedure just described is used to account for correlation lengths. The correlation lengths for two or three dimensional orientations are not significantly different than those measured in Lennard-Jones-type clusters.[35–41,43–45]

For most sizes, a linear temperature schedule with $n_w=40$ walkers,

$$T_i = T_{\min} + T_{\max}\left(\frac{i-1}{n_w-1}\right), \tag{36}$$

and with $T_{\min}=10$ K and $T_{\max}=300$ K is sufficient. We verify that the energy at the coldest temperatures extrapolates to values reasonably close to the energy of the global minimum. Then, we check that the heat capacity approaches the equipartition value, $(6n-3)$ for n nonlinear rigid bodies. The classical simulations of the octamer and hendecamer obtained with the linear temperature schedule in Eq. (36) are not satisfactory. The heat capacity of both systems does not approach equipartition, and large fluctuations at cold temperatures are observed. We repeat the classical parallel tempering simulations for these two systems a number of times as we attempt to optimize n_w, $T_{\max}$ and $T_{\min}$.

Eventually, for the octamer and the hendecamer a new temperature series designed to grow geometrically with $n_w=60$ walkers is adopted,

$$T_i = T_{\min}\left(\frac{T_{\max}}{T_{\min}}\right)^{(i-1)/(n_w-1)}, \tag{37}$$

with $T_{\min}=0.5$ K and $T_{\max}=300$ K. A new classical simulation with the temperature schedule in Eq. (37) yields a reproducible heat capacity curve that approaches the equipartition value and a value for the energy at 0.5 K statistically identical to the energy of the global minimum for the octamer. However, for the hendecamer we find large fluctuations in the heat capacity at low temperatures. We determine that, below 2 K, the random walk is trapped into a high energy well, since the energy fluctuates above that of the global minimum and does not extrapolate to the global minimum value at $T\rightarrow 0$. We repeat the classical parallel tempering simulation of the hendecamer several times with a random initial configuration for all the walkers and we experiment with different values of $T_{\min}$ and $T_{\max}$. Ultimately, to obtain sensible and reproducible results for the energy and heat capacity of the hendecamer, we have to seed each walker with the global minimum configuration. For the classical simulation we use the nonlinear temperature schedule in Eq. (37), whereas for all the path integral simulations, we find the linear temperature schedule with $n_w=40$ walkers in Eq. (36) adequate. A comparison of the seeded and unseeded quantum simulation with $k_{\max}=32$ displays small but significant differences in the heat capacity in the lowest five temperatures.

Path integral simulations require careful tuning of the number of series coefficients k_m. High temperature simulations are classical or nearly classical and only require a relatively small number of coefficients. As the temperature decreases, the quantum effects grow in magnitude and the number of coefficients required to achieve convergence increases accordingly. The heat capacity of the ammonia dimer is shown Fig. 1 for several values of k_m. The data sets in Fig. 1 are produced with the purpose of studying the convergence properties of the heat capacity estimator. The classical ($k_m=0$) and all the quantum simulations agree, within the statistical error, at 300 K. The $k_m=24$, 32, and 40 and $k_m=40$ data points are hard to distinguish for most but the coldest temperatures. From the graph in Fig. 1 we deduce that a $k_m=32$ simulation is converged within the statistical error for

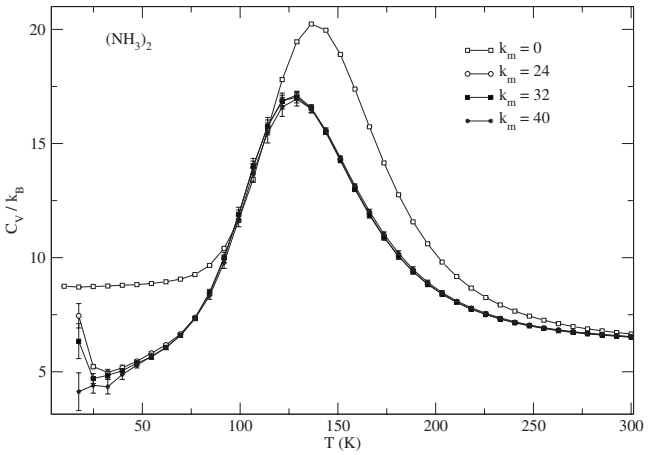

FIG. 1. The heat capacity of the ammonia dimer for several values of k_m. The white squares are the classical limit. The peak at 130 K in the classical heat capacity is associated with the dissociation "phase change," The k_m =24, 32, and 40 curves are statistically identical for all temperatures above 20 K.

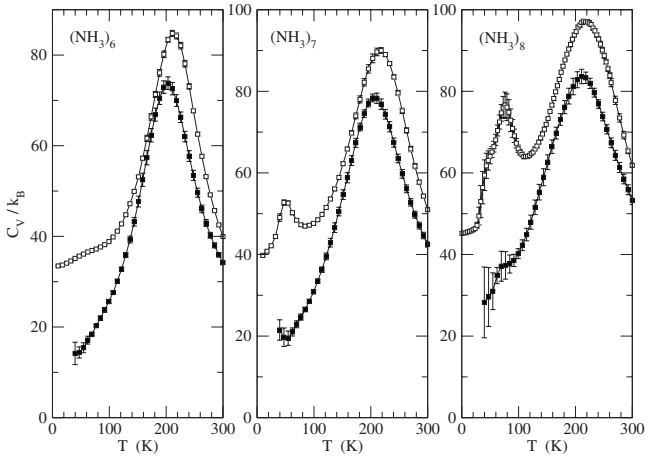

FIG. 3. The heat capacity of the ammonia hexamer to the octamer. The white squares are classical k_m=0 results, and the black squares are k_m=32 results. The heptamer has a distinct melting peak in the classical heat capacity at 40 K, whereas the octamer has an intense melting peak at 75 K and a shoulder at 50 K in the classical heat capacity.

$T \geq 40$ K. We use $k_m=32$ for the simulations of all the remaining clusters, and we report quantum results for temperatures equal to and greater than 40 K.

In Fig. 2(a), we graph the binding energy per ammonia molecule for $(NH_3)_2$ through $(NH_3)_{11}$. The white squares are obtained by using the three lowest values of $\langle E \rangle$ from the classical simulation. We use the energy data at the three lowest temperatures (10.0, 17.4, and 24.9 K) to extrapolate the $T=0$ K limit. For the heptamer, octamer, and hendecamer, we use the value of the energy at 0.5 K. The black squares are estimates of the actual binding energy obtained from the quantum simulations at 40 K. Trends in the graphs of the total energy obtained with $k_m=32$ for all ten systems indicate that the energy is approaching the ground state. Both the classical and the quantum simulations indicate a gradual increase in stability with growing size. We use the quantum energy at 40 K as a crude estimate of the zero point energy. This is 55% of the total binding energy for the dimer, drops from the dimer to the trimer, and flattens out to about 37% of the binding energy for the tetramer and beyond.

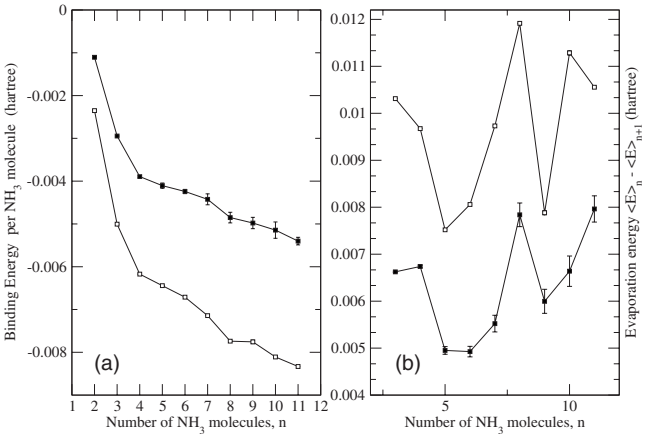

FIG. 2. (a) The classical and quantum binding energies per ammonia molecule in the dimer to hendecamer range. (b) The classical and quantum evaporation energies in the dimer to hendecamer range. The white squares are $T \rightarrow 0$ extrapolations of classical parallel tempering simulations. The black squares are values of the energy at 40 K from $k_m=32$ simulations.

An alternative representation of the energy results is provided by Fig. 2(b), where the monomer evaporation energy $(\langle E \rangle_{n-1} - \langle E \rangle_n)$ is shown as a function of the number of monomers n in the parent cluster. As expected, the inclusion of quantum effects reduces substantially the energy needed to dissociate a monomer from the parent species (roughly 25%) due to the confinement of molecular librational motion. Bearing in mind the connection highlighted in Ref. 57 between $\langle E \rangle_{n-1} - \langle E \rangle_n$ and the appearance of magic number clusters in the evaporative ensemble, the substantial reduction in the binding energy for the ammonia clusters clearly stresses the need for a quantum treatment of light systems such as $(NH_3)_n$ to obtain an accurate prediction of fragmentation lifetimes. In retrospective, a similar finding also applies to $(HF)_n$ (Ref. 41) and to $H^+(H_2O)_n$.[43,44] A more detailed comparison of the data shown in Fig. 2(b) also indicates that quantum and, to some extent, thermal effects tend to smooth the roughed behavior shown by the minimum energy results, with the evaporation energy of $(NH_3)_8$ and $(NH_3)_9$ being, respectively, decreased and increased. Although it is difficult to disentangle the quantum contribution to this finding from the thermal one, a survey of the local minima energy landscape provided in Ref. 29 suggests the decrease in the evaporation energy of the octamer to be primarily due to its compact and stiff distorted cubic structure, well separated from the second low lying isomer. For the nonamer, a similar analysis is hampered by the presence of many low lying minima very close in energy to the global minimum. In this case, the possibility for the system to have a sizable population in those minima prevents us from suggesting possible contributions to its improved stability toward dissociation, apart from what is already discussed for the octamer, and the possible gain in free energy due to a higher entropy for $n=9$ than $n=8$.

The heat capacities of the hexamer through the hendecamer are in Figs. 3 and 4. In all six graphs, we use white

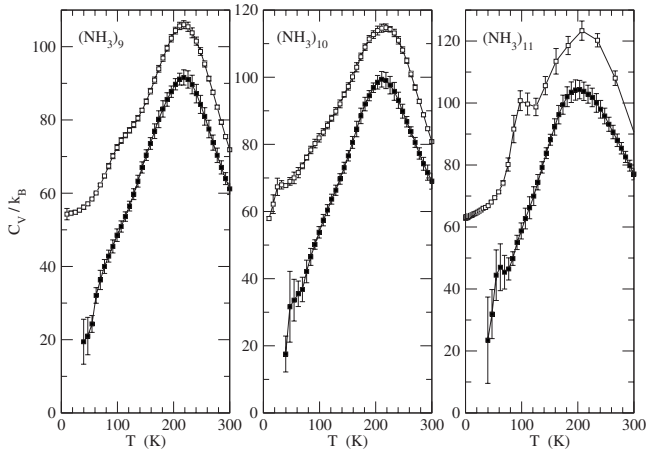

FIG. 4. The heat capacity of the ammonia nonamer through the hendecamer. The white squares are classical $k_m=0$ results, and the black squares are $k_m=32$ results.

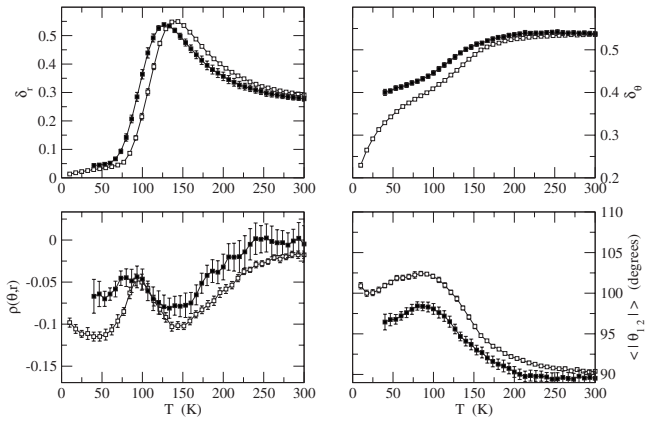

FIG. 5. The structural properties of the dimer as functions of temperature. The white squares are classical $k_m=0$ results, and the black squares are $k_m=32$ results.

squares for the classical results and black squares for the converged quantum results. The dominant feature in the classical and quantum heat capacities of the ten clusters is the "boiling" peak. The conspicuous boiling feature peaks at 140 K for the dimer and between 200 and 220 K for the rest of the systems. The corresponding quantum peaks are relatively less intense and slightly shifted to colder temperatures by 5 K or less. The quantum effects below the 300 K range are substantial for all the ten systems. Noteworthy is also the fact that the difference between the quantum and classical heat capacities at 300 K increases monotonically as a function of the number of molecules in the cluster n, with a slope of ≈ 1.5 units of k_B. Clearly, the trend is the result of the increase in the number of confined librational degrees of freedom behaving quantistically at 300 K. However, the trend is not linear, especially in the dimer through the heptamer range. Other factors contribute to shifts in the differences. The boiling peaks in the classical heat capacity progress irregularly toward higher temperatures and gradually broaden as a function of size in this range.

The classical heat capacities of the dimer through the pentamer (not shown) are featureless in the 0–100 K range; they approach smoothly and with small statistical fluctuations the expected equipartition values as the temperature decreases. The quantum heat capacities of the dimer through the pentamer are also featureless in the 0–100 K range and are smoothly and monotonically decreasing functions of temperature, with small statistical fluctuations for all but the coldest one or two temperature points.

The heat capacities of the hexamer through the hendecamer are rich with features at colder temperatures, indicating the presence of melting and perhaps other kinds of phase changes. The pattern of the peaks below the boiling range for the hexamer through the hendecamer resembles vaguely the peak progression observed in Lennard-Jones clusters in the 4–60 range by Frantz.[80,81] However, the progression of the melting peak takes place much more irregularly and rapidly as the size increases. The most subtle melting signature is observed in the classical heat capacity of the hexamer. The heat capacity of the hexamer is on the left panel in Fig. 3. Close inspection of the graph of $k_B^{-1}[C_V(T_i) - C_V(T_{i-1})]$ (not shown) and its error bars reveals a statistically significant feature between 40 and 60 K. The heptamer has a distinct melting peak at 50 K in the classical heat capacity. The quantum heat capacities for the hexamer and the heptamer are featureless. The $k_m=32$ heat capacity of the heptamer increases a statistically significant amount as the temperature drops from 60 to 40 K. However, there is no sufficient evidence to confirm the presence of a melting feature in the quantum heat capacity of the heptamer. The classical heat capacity of the octamer has an intense melting peak at 75 K and a shoulder at 50 K. The quantum heat capacity shows a much less intense but nevertheless statistically significant feature at 60 K. The changes in the slope of C_V/k_B computed with $k_m=32$ for the octamer occur in a range of temperatures where we can exclude convergence artifacts with confidence.

The evidence of melting in both the classical heat capacities of the nonamer and decamer, again, are subtle but significant. Their respective quantum heat capacities have less intense features. The statistical fluctuations at the lowest five temperature points preclude us from extracting any significance from the small undulations visible in the left and central graph of Fig. 4. By contrast, the hendecamer shows a relatively intense melting shoulder at 100 K in the classical heat capacity and a less intense but statistically significant feature shifted toward colder temperatures by more than 40 K in the quantum limit.

B. Structural analysis

The structural features of the dimer are in Figs. 5 and 6. In Fig. 5, the top left panel contains the Lindemann index for the fluctuations of the radial degrees of freedom; the top right panel is the angular Lindemann index defined in Eq. (31). The bottom left is a graph of the correlation coefficient between the radial and the angular degrees of freedom, and the bottom right is a graph of the average absolute angle between the two C_3 axis of the ammonia dimer, $\langle|\theta_{12}|\rangle$. Classical and quantum results are compared. As with all the other graphs, we use white squares for classical simulations and black squares for quantum ($k_m=32$) simulations. The radial

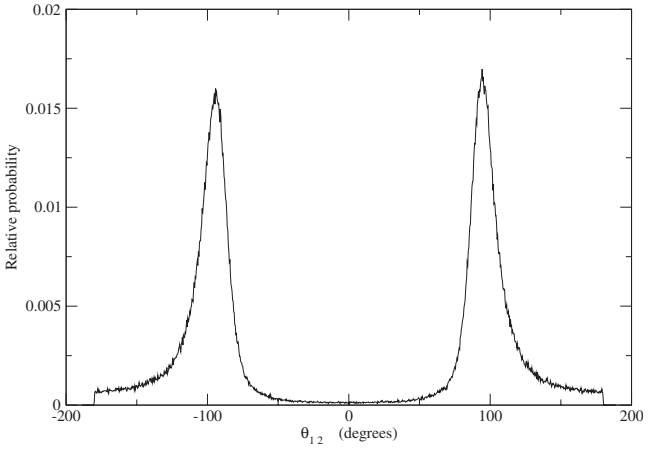

FIG. 6. The distribution of the angle between the two C_3 axes of the ammonia dimer at 10 K from the classical simulation. The double feature of this distribution is the result of the donor-acceptor exchange that takes place in the classical simulation at 10 K.

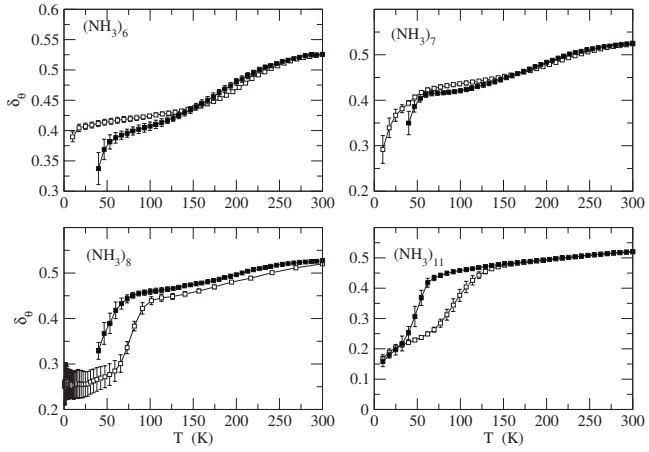

FIG. 8. The angular Lindemann index [cf. Eq. (31)] as a function of temperature for the hexamer, heptamer, octamer, and hendecamer. The white squares are classical and the black squares are quantum results.

Lindemann index δ_r increases sharply from 75 to 150 K from values around 0.05 to values one order of magnitude larger. It then drops gradually and approaches a plateau around 0.3. Its quantum equivalent has the same shape and values close to the classical ones at the low and high temperature ends but increase sharply 15 K below the sharp rise in the classical δ_r. The change in δ_r correlates with the dissociation of the dimer. As previously reported for Lennard-Jones systems,[67] quantum delocalizations play the same role as thermally induced transitions. This explains why the quantum δ_r rises at lower temperatures compared to its classical counterpart. The angular Lindemann index δ_θ (on the top right of Fig. 5) on the other hand shows substantial quantum effects at cold temperatures and does not drop from a maximum at high temperature. Instead, both the quantum and classical δ_θ approach a plateau around 0.54. The correlation coefficient $\rho(\theta,r)$ is small and negative and is a weak function of temperature. The differences between the classical and quantum values $\rho(\theta,r)$ are relatively small throughout the whole temperature range. Finally, the classical and quantum average values of $|\theta_{12}|$ increase gradually to a maximum at 90 K then drop and flatten out around 90° at high temperature. Figure 6 contains the distribution of the angle θ between the two C_3 axes of the dimer at 10 K from a classical simulation. The distribution is clearly bimodal containing equal amounts of donor-acceptor and acceptor-donor configurations for the dimer and presenting a low occupation probability in the region of donor-acceptor exchange. However, the high value of the angular Lindemann index obtained at low temperature from the quantum simulation for this system is a clear indication of a broad distribution for the angle between the two C_3 axis, the latter suggesting the presence of the highly fluxional behavior previously highlighted in the literature.[20]

We single out the hexamer, heptamer, octamer, and hendecamer for in depth structural analysis because they display the most interesting thermodynamic behavior in Figs. 3 and 4. (However, *vide infra* for a discussion on $n=3$, 4, and 5.) The radial Lindemann index δ_r, the angular Lindemann index δ_θ, and the correlation coefficient between the radial and relative orientation degrees of freedom $\rho(\theta,r)$ for the hexamer, heptamer, octamer, and hendecamer are in Figs. 7–9, respectively. Both the classical and quantum δ_r increase with

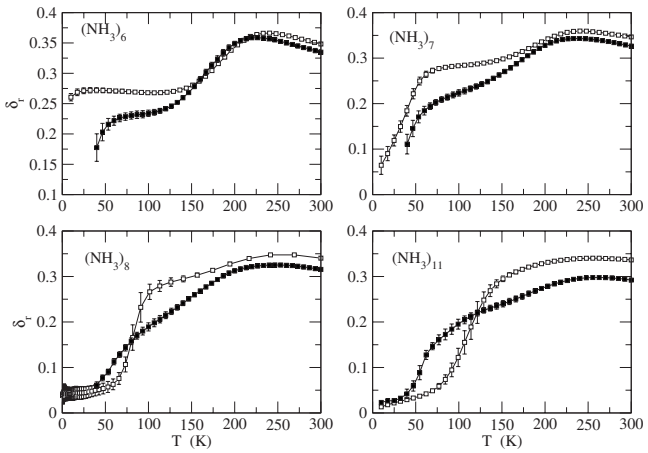

FIG. 7. The radial Lindemann index [cf. Eq. (30)] as a function of temperature for the hexamer, heptamer, octamer, and hendecamer. The white squares are classical and the black squares are quantum results.

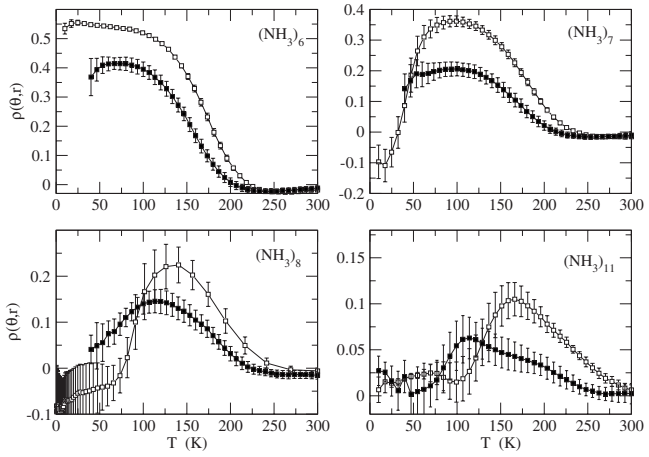

FIG. 9. The correlation coefficient between orientation and radial degrees of freedom [cf. Eq. (32)] as a function of temperature for the hexamer, heptamer, octamer, and hendecamer. The white squares are classical and the black squares are quantum results.

temperature and show sharp changes that correlate with melting and boiling changes. Despite these similarities, the behavior of δ_r for the hexamer and heptamer is at partial variance with the one displayed by the octamer and hendecamer, the low temperature quantum results for $(NH_3)_{6,7}$ being lower than the classical ones. To investigate qualitatively this behavior we have characterized structurally the quantum and classical walks at 40 K as in Sec. IV. The counterintuitive behavior δ_r for the hexamer and heptamer is due to the juxtaposition of two effects, namely, the presence of a low temperature phase change in the classical simulations, evident in Fig. 3, and the fact that the system free energy surface, when quantum effects are included, is characterized by a small number of wells. For the hendecamer, the melting and dissociating temperatures are relatively close in the classical limit. It is therefore difficult to resolve the melting and boiling in the rise in δ_r in the classical limit for the hendecamer. In the quantum limit, however, δ_r for the hendecamer has two distinct features, since the peak temperatures are well separated. It is interesting to note that δ_r is larger in the quantum limit at low temperature due to quantum fluctuations ($T<40$ K) and the phase change (40 K$<T<$120 K), and that the quantum effects are large. A similar behavior, albeit less marked, is also present in the plot of the Lindemann index for the octamer.

The angular Lindemann index δ_θ in Fig. 8 displays the same sharp changes, though less pronounced than in δ_r, suggesting that the correlations among the two sets of degrees of freedom are significant. The quantum effects are smaller for δ_θ compared to those in δ_r, in sharp contrast with what we see for the dimer, for which the quantum effects are larger for the relative orientation. Apparently, the angular Lindemann index δ_θ is more sensitive to melting changes than evaporations as evidenced by the strict correlation between the temperature where its sudden increase begins and the melting peak present in the heat capacity plots for the octamer and hendecamer. The correlation coefficients $\rho(\theta,r)$ are also different for the larger systems compared to the dimer's. In the dimer the correlation is small and negative. For the larger clusters the correlation is positive and it is a nontrivial function of temperature. With some exception, quantum effects diminish the correlations among the angular and radial degrees of freedom. $\rho(\theta,r)$ drops to zero in magnitude at high temperature for all the sizes. It drops exponentially to zero as the temperature increases beginning at values where the heat capacity rises toward the boiling peak. The correlation coefficients $\rho(\theta,r)$ for the hendecamer behave differently from all the other sizes. Both classical and quantum values of $\rho(\theta,r)$ for the hendecamer start out small and positive, grow to relatively moderate and positive values, and decrease to zero toward higher temperatures.

To gain a deeper understanding of the melting changes observed for the heptamer, octamer, and hendecamer, we collect two additional sets of distributions. Ten independent classical walks with 10^6 "warm up" moves followed by 10^5 moves are performed. During the second part of the walk, all 10^5 configurations are written to disk and later used to obtain histograms of the potential energy and the SCA distance from the global minimum defined in Eq. (35). The histograms for the potential energy of the heptamer, octamer, and hendecamer at selected temperatures are shown in Fig. 10. The middle panel of Fig. 10 contains the normalized distributions of the potential energy of the octamer. The temperatures are chosen to be slightly above the shoulder in the heat capacity and above the melting peak of the heat capacities. The distribution of V for the octamer at 42.6 K is darkened to make evident its bimodal nature, with an intense peak at -0.059 hartree and a second weaker peak at -0.055 hartree. For the heptamer and the hendecamer, we choose to display the distributions at temperature that are below and above the melting feature of the heat capacity. As we graph all the distributions for the heptamer and the hendecamer, we observe the typical moderately asymmetric shapes about the maximum, with slightly elongated tails toward higher values. The distributions for the heptamer and the hendecamer display a gradual broadening and shifting of the peaks to higher values of the potential. The only exception we observe is the distribution at 126 K for the hendecamer, where a more pronounced asymmetric nature could suggest two unresolved contributions.

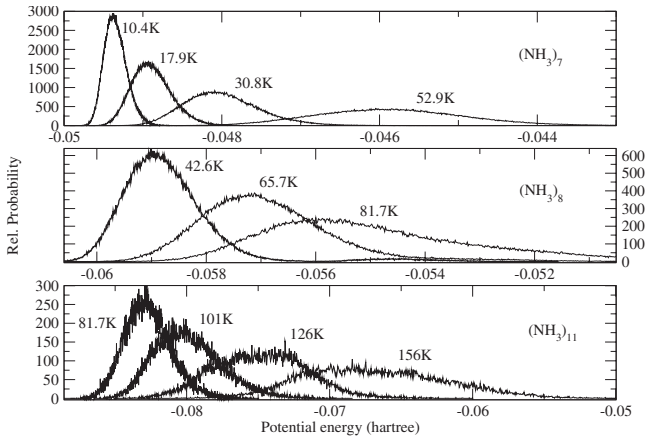

FIG. 10. Distributions of the potential energy at several temperatures from classical simulations for the heptamer (top panel), octamer (middle panel), and hendecamer (lower panel).

In Fig. 11, selected distributions for Δ_0 for the hen-

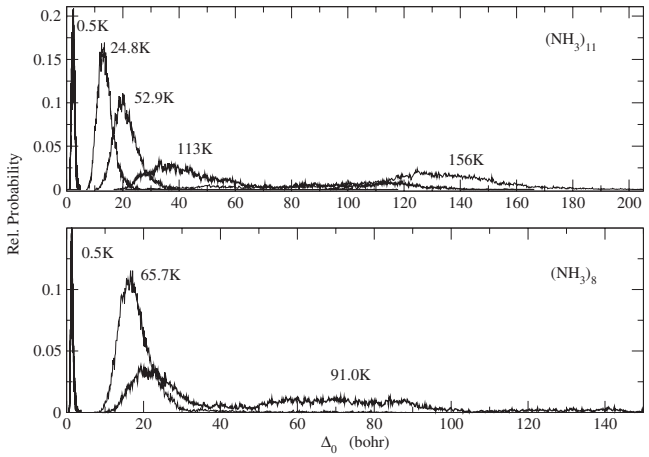

FIG. 11. Distributions of the SCA distance from the global minimum [cf. Eq. (35)] at several temperatures from classical simulations for the hendecamer (top panel) and the octamer (bottom panel).

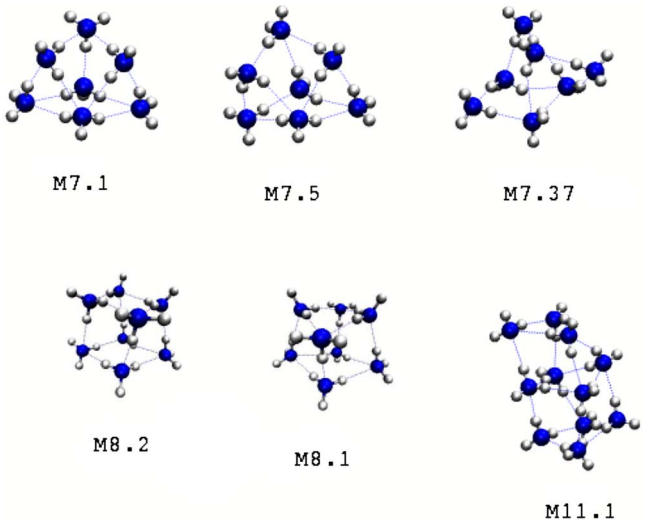

FIG. 12. Several representative structures for the heptamer, octamer, and hendecamer. The label $M_{n.l}$ is used to identify a minimum of a cluster of size n and its energetic ranking l starting with $l=1$ for the global minimum. $M_{8.1}$ is the global minimum of the octamer. The distorted cube has D_{2d} symmetry, and is displayed with the ring plane facing up. The Up-Down-Up-Down orientation of the free NH bonds on the plane of the ring can be easily seen. $M_{8.2}$ is the second minimum of the octamer displayed with the ring plane facing up and showing the Up-Up-Down-Down orientation of the free NH bonds on the plane of the ring.

decamer and the octamer are plotted. In the case of the octamer, we observe a shoulder on the melting peak in the C_V plot, which could be the result of a solid-solid change taking place. One could hypothesize the existence of a clean solid-solid change between two or more minima of the PES. Distributions of Δ_0 are distinctly bimodal when solid-solid transitions give rise to features in the thermodynamic variables.[82] Instead, the distributions of Δ_0 for the octamer begin with a relatively sharp and slightly asymmetric peak near zero at temperatures below 1 K. Therefore, we conclude that there are no solid-solid phase changes taking place a low temperature for the octamer. The peak maximum gradually shifts toward larger values of Δ_0 as the distributions become broader. At temperatures slightly below the melting peak in the C_V plot, a much broader and barely significant tail toward larger values of Δ_0 grows gradually, producing eventually a highly asymmetric distribution with several peaks. From 10^5 configurations of the octamer obtained at 47.5 K, we find only three structures for which $\Delta_0 > 35$ bohrs. We subjected these to the Brownian dynamics at 0 K, presented in Sec. II D, and we obtain isomer $M_{8.2}$ displayed in Fig. 12. The notation used here and in the captions of Fig. 12 is $M_{n.l}$, where n is the number of ammonia molecules and l is the energy ranking of the minimum with 1 for the global minimum, etc.

The distributions of Δ_0 for the heptamer (not shown) and the hendecamer (top panel of Fig. 11) behave in a similar way to the octamer ones. In Fig. 12 we display the C_{2v} global minimum of the heptamer ($M_{7.1}$) along with two minima that were isolated at 40 K as the cluster is melting. Both $M_{7.5}$ and $M_{7.37}$ are distorted defective pentagonal bipyramids. The melting range for the heptamer is characterized for the most part by a number of closely related compact structures, although occasional open, nearly planar structures are observed as well. The results observed when the melting range of the octamer and the hendecamer are analyzed in this manner are similar to those for the heptamer. In Fig. 12 we display the global minimum of the hendecamer ($M_{11.1}$), which dominates the thermodynamics below 90 K. In the molten range, between 40 and 100 K, the peak associated with the global minimum contributes increasingly less until it completely disappears.

All the distributions of Δ_0 in Fig. 11, except for those at 0.5 K, are normalized, so that the area under the curves is 1. The distribution at 0.5 K for the hendecamer is divided by 4, and the same distribution for the octamer is divided by 10. We do this to bring all the plots on the same scale, so that sufficient details of the tail toward high values are visible. At the same time, Fig. 11 contains a visible confirmation that the walk settles in the global minimum if the temperature is sufficiently cold.

Given the difficulties we encounter in simulating the hendecamer, even in the classical range, we perform a number of additional computations. First, we run the genetic algorithm for 30 generations. The method we use is briefly introduced in Sec. II E. Quenching takes place with Brownian dynamics at 0 K, developed in Sec. II D. The quenched children are sorted and compared with the minima at hand by a second program that uses the SCA. This last step ensures that the next generation of parents, selected from the top 100 in the sorted list in ascending energy, is of distinct structures. Using this procedure we produce more than 2000 distinct minima. We stop searching for minima after 30 consecutive generations fail to find a global minimum lower than what is reported in Ref. 29. We find many optically active minima, distinguished by SCA, as nonsuperimposable pairs of structures with identical energies. At the end of the genetic algorithm run, we select the lowest nine isomers (which include two sets of enantiomers) and we explore the potential energy landscape further using dynamic runs. These dynamic runs, initiated by distorting the minima, are used for two purposes. First, we find it prudent to confirm with an independent exploration of the PES that we have indeed obtained the lowest energy structure since we initiate the classical parallel tempering of the hendecamer from its global minimum. Second, we speculate that the PES for $(NH_3)_{11}$ may have unusually high barriers surrounding the global minimum; however, after inspecting a number of trajectories, we find that with relatively small excess energies trajectories end up in different minima from where the dynamics are initiated.

IV. CONCLUSIONS

In the present article we report the results of a number of simulations of ammonia clusters in the dimer through the hendecamer range. We observe that the binding energy per ammonia molecule is a monotonically decreasing function of size. The quantum effects on the binding energy per ammonia molecule are large. We estimate that the zero point energy is approximately 35% of the binding energy for the largest sizes and climbs as we move toward smaller sizes to 50% for the dimer. From the smooth behavior of the binding

energy per molecule in the dimer through the hendecamer range, one would be tempted to conclude that there are no conspicuous magic numbers both in the classical or quantum limit of the binding energy. A slightly larger change in the binding energy from the heptamer to the octamer is nevertheless present in the classical binding energy, albeit the change is much smaller than what is observed for magic number sizes in homogeneous Lennard-Jones clusters.[80,81] However, the differential quantity provided by the quantum evaporation energy presents a rougher behavior than the total binding energy, suggesting the possibility of an enhanced kinetic stability (i.e., a longer lifetime) for the octamer with respect to the other clusters. It is our opinion that this issue, which embraces also species such as $(HF)_n$ and $H^+(H_2O)_n$, deserves a more careful study currently outside the scope of this work.

A direct comparison between our results and experimental data[5,9,12] is complicated by the lack of information on the internal temperature of the clusters and by the rigid molecular model employed in the simulations. Nevertheless, the behavior of C_V, δ_r, and δ_θ with respect to T for $(NH_3)_{2-6}$ (not shown for $n=3-5$) seems to support the idea of a more fluxional, or flexible, nature for the dimer, pentamer, and hexamer suggested in Refs. 6–9 and 12. For the dimer this is justified by the facile donor-acceptor exchange indicated in Fig. 6 and by the high δ_θ values. Such behavior for $(NH_3)_{5,6}$ is produced by the smaller energy gap separating their lowest energy isomer from the one lying just above than in the case of $(NH_3)_{3,4}$.[29] Similarly, the results for the evaporation energy obtained from our quantum simulations and inferred from experiments[12] agree in indicating $(NH_3)_5$ and $(NH_3)_6$ as less stable with respect to dissociation than neighbor species. We emphasize that both the energetic and structural features just mentioned are not in contradiction with the possibility for $n=6$ of presenting a single well free energy surface. In fact, a shallow well explains both the relatively higher classical values of $\delta_{r,\theta}$ for $n=6$ than for $n=3$, 4, and 7–11 and the finding that the radial and angular Lindemann indices obtained using quantum simulation are lower than the classical counterparts (Fig. 7).

There are no distinct solid-solid transitions for $(NH_3)_8$ despite the indications in the C_V plot. The structural analysis does not yield sufficient evidence that the $M_{8.1}$-$M_{8.2}$ isomerization is separated from the melting phase. We do not observe the characteristic bimodal distribution in the SCA measure Δ_0. Rather, around the melting peak for $(NH_3)_{7,8}$ and $(NH_3)_{11}$ we find a large number of structures of all kinds (e.g., $M_{7.5}$ and $M_{7.35}$ in Fig. 12).

In homogeneous Lennard-Jones clusters,[80,81] there is a clear correlation between the thermodynamic stability computed with the binding energy and the energy differences between the global minimum and the higher energy isomers (minima in the PES). A relatively large difference between the global minimum and the higher energy isomers creates distinct melting features in the classical heat capacity. Figure 3 demonstrates that the ammonia octamer does have the most prominent melting feature in the classical heat capacity, and this is consistent with the pattern of energy of the minima.[29] The quantum effects on the heat capacity are substantial as Figs. 1, 3, and 4 show. Holonomic constraints for the internal modes of each ammonia molecule and the machinery of the stereographic projection coordinate map as the parametric representation of the inhomogeneous Galilean group afford us the benefits of the cubic convergence that the reweighted random series expansion provides for path integrations. Without holonomic constraints, path integral simulations of molecular matter are difficult at room temperature, the upper limit in our simulations, since even at those relatively elevated temperatures, the ground state dominates the thermodynamic contributions from the internal degrees of freedom.

The fact that we find difficulties in simulating $(NH_3)_{11}$ with classical parallel tempering indicates the degree of complexity of the underlying PES. Since the classical parallel tempering simulations need a warm up walk much longer than 10^6 moves, irrespective of temperature schedule, we have less confidence in the global minimum search. Consequently, we repeat it with two separate strategies. We generate and quench additional 3000 minima with the genetic algorithm and we use the lowest nine structures as starting points for 3600 trajectories with a range of excess energies. The dynamic data help us reject the hypothesis that the global minimum of the hendecamer is surrounded by unusually high barriers.

The structural analysis of the ten independent parallel tempering walks for the heptamer, octamer, and hendecamer indicates that the global minimum has by far the largest volume of phase space and that all the other minima contribute individually by a statistically insignificant amount regardless of the presence or lack of funneled structures. Nevertheless, the numerical difficulties we encounter are unsettling. We repeat the classical parallel tempering simulations for numerous sizes to compare seeded versus unseeded simulations without finding any significant difference besides those produced by the hendecamer. These observations have compelled us to initiate a thorough characterization of the PES of the hendecamer to see what lessons, if any, can be learned. Unfortunately, the characterization of the $(NH_3)_{11}$ PES in the present work is not sufficient. A search for the transition states and several basin hopping simulations seem justifiable to us. We have decided not to lengthen the presentation of the present work any further at this time.

ACKNOWLEDGMENTS

Acknowledgment is made to the donors of the Petroleum Research Fund, administered by the ACS (Grant No. 41846-B6) for partial support of this research. This work has also been supported, in part, by the National Science Foundation (Grant No. CHE0554922). Support is also gratefully acknowledged from The Stacy Ann Vitetta '82 Professorship Fund and The Ellington Beavers Fund for Intellectual Inquiry from Arcadia University. M.M. acknowledges an EPSRC-GB Advanced Research Fellowship (Grant No. GR/R77803/01).

[1] T. Kurtén, L. Torpo, C.-G. Ding, H. Vehkamäki, M. R. Sundberg, K. Laasonen, and M. Kulmala, J. Geophys. Res. **112**, D04210 (2007).
[2] P. M. Pawlowski, S. R. Okimoto, and F.-M. Tao, J. Phys. Chem. A **107**, 5327 (2003).

[3] Device for operating internal combustion engines with mixtures of ammonia, hydrogen, and nitrogen prepared from ammonia, M. Zavka, U.S. Patent No. 2140254, December 13th (1938).
[4] A. W. Hewat and C. Riekel, Acta Crystallogr., Sect. A: Cryst. Phys., Diffr., Theor. Gen. Crystallogr. **35**, 569 (1979).
[5] J. A. Odutola, T. R. Dyke, B. J. Howard, and J. S. Muenter, J. Chem. Phys. **70**, 4884 (1979).
[6] D. D. Nelson, Jr., G. T. Fraser, and W. Klemperer, J. Chem. Phys. **83**, 6201 (1985).
[7] D. D. Nelson, Jr., W. Klemperer, G. T. Fraser, F. J. Lovas, and R. D. Suenram, J. Chem. Phys. **87**, 6364 (1987).
[8] S. Süzer and L. Andrews, J. Chem. Phys. **87**, 5131 (1987).
[9] M. Snels, R. Fantoni, R. Sanders, and W. L. Meerts, Chem. Phys. **115**, 79 (1987).
[10] M. N. Slipchenko, B. G. Sartakov, and A. F. Vilesov, J. Chem. Phys. **128**, 134509 (2008).
[11] C. Steinbach, U. Buck, and T. A. Beu, J. Chem. Phys. **125**, 133403 (2006).
[12] F. Huisken and T. Pertsch Chem, Physica (Amsterdam) **126**, 126 (1988).
[13] M. Marchi, M. Sprik, and M. L. Klein, J. Chem. Phys. **89**, 4918 (1988).
[14] S. M. Cybulski, Chem. Phys. Lett. **228**, 451 (1994).
[15] J. S. Lee and S. Y. Park, J. Chem. Phys. **112**, 230 (2000).
[16] J. Stålring, M. Schütz, R. Lindh, G. Karlstrom, and P.-O. Widmark, Mol. Phys. **100**, 3389 (2002).
[17] T. A. Beu and U. Buck, J. Chem. Phys. **114**, 7853 (2001).
[18] T. A. Beu, C. Steinbach, and U. Buck, J. Chem. Phys. **117**, 3149 (2002).
[19] T. A. Beu and U. Buck, J. Chem. Phys. **114**, 7848 (2001).
[20] E. H. T. Olthof, A. van der Avoird, and P. E. S. Wormer, J. Chem. Phys. **101**, 8430 (1994).
[21] K. P. Sagarik, R. Ahlrichs, and S. Brode, Mol. Phys. **57**, 1247 (1986).
[22] A. Hinchliffe, D. G. Bounds, M. L. Klein, I. R. McDonald, and R. Righini, J. Chem. Phys. **74**, 1211 (1981).
[23] G. Duquette, T. H. Ellis, G. Scoles, R. O. Watts, and M. L. Klein, J. Chem. Phys. **68**, 2544 (1978).
[24] R. W. Impey and M. L. Klein, Chem. Phys. Lett. **104**, 579 (1984).
[25] I. R. McDonald and M. L. Klein, J. Chem. Phys. **64**, 4790 (1976).
[26] M. L. Klein, I. R. McDonald, and M. Righini, J. Chem. Phys. **71**, 3673 (1979).
[27] J. A. Northby, J. Xie, D. L. Freeman, and J. D. Doll, Z. Phys. D: At., Mol. Clusters **12**, 69 (1989).
[28] P. E. Janeiro–Barral and M. Mella, J. Phys. Chem. A **110**, 11244 (2006).
[29] P. E. Janeiro-Barral, M. Mella, and E. Curotto, J. Phys. Chem. A **112**, 2888 (2008).
[30] R. P. Feynman, Rev. Mod. Phys. **20**, 367 (1948).
[31] B. S. DeWitt, Rev. Mod. Phys. **29**, 377 (1957).
[32] L. S. Schulman, *Techniques and Applications of Path Integration* (Wiley, New York, 1981).
[33] S. Weinberg, *The Quantum Theory of Fields* (Cambridge University Press, Cambridge, 1996), Vol. 1.
[34] H. Kleinert, *Path Integrals in Quantum Mechanics, Statistics and Polymer Physics* (World Scientific, Singapore, 1990).
[35] M. F. Russo, Jr. and E. Curotto, J. Chem. Phys. **118**, 6806 (2003).
[36] M. F. Russo, Jr. and E. Curotto, J. Chem. Phys. **120**, 2110 (2004).
[37] M. W. Avilés and E. Curotto, J. Chem. Phys. **122**, 164109 (2005).
[38] E. Curotto, J. Chem. Phys. **123**, 134102 (2005).
[39] S. F. Langley, E. Curotto, D. L. Freeman, and J. D. Doll, J. Chem. Phys. **126**, 084506 (2007).
[40] M. W. Avilés, M. L. McCandless, and E. Curotto, J. Chem. Phys. **128**, 124517 (2008).
[41] M. W. Avilés, P. T. Gray, and E. Curotto, J. Chem. Phys. **124**, 174305 (2006).
[42] G. A. Voth, D. Chandler, and W. H. Miller, J. Chem. Phys. **91**, 7749 (1989).
[43] M. Mella and D. C. Clary, J. Chem. Phys. **119**, 10048 (2003).
[44] M. Mella, D. C. Clary, J.-L. Kuo, and M. L. Klein, Phys. Chem. Chem. Phys. **7**, 2324 (2005).
[45] E. Curotto, D. L. Freeman, and J. D. Doll, J. Chem. Phys. **128**, 204107 (2008).
[46] R. A. Kuharski and P. J. Rossky, J. Chem. Phys. **82**, 5164 (1985).
[47] D. Marx and M. H. Müser, J. Phys.: Condens. Matter **11**, R117 (1999).
[48] D. Marx and P. Nielaba, Phys. Rev. A **45**, 8968 (1992).
[49] T. F. Miller and D. C. Clary, J. Chem. Phys. **116**, 8262 (2002).
[50] C. Predescu, e-print arXiv:cond-mat/0302171.
[51] C. Predescu, D. Sabo, and J. D. Doll, J. Chem. Phys. **119**, 4641 (2003).
[52] C. Predescu and J. D. Doll, J. Chem. Phys. **117**, 7448 (2002).
[53] C. Predescu, D. Sabo, J. D. Doll, and D. L. Freeman, J. Chem. Phys. **119**, 10475 (2003).
[54] C. Predescu, D. Sabo, J. D. Doll, and D. L. Freeman, J. Chem. Phys. **119**, 12119 (2003).
[55] D. Sabo, C. Predescu, and J. D. Doll, J. Chem. Phys. **121**, 856 (2004).
[56] C. Predescu, P. A. Frantsuzov, and V. A. Mandelshtam, J. Chem. Phys. **122**, 154305 (2005).
[57] F. Calvo and P. Parneix, J. Chem. Phys. **126**, 034309 (2007).
[58] W. D. Curtis and F. R. Miller, *Differential Manifolds and Theoretical Physics* (Academic, New York, 1985).
[59] R. Gilmore, *Lie Groups, Lie Algebras, and Some of Their Applications* (Dover, New York, 2006).
[60] L. Zheng, S.-N. Luo, and D. L. Thompson, J. Chem. Phys. **124**, 154504 (2006).
[61] G.-J. Guo, Y.-G. Zhang, Y.-J. Zhao, K. Refson, and G.-H. Shan, J. Chem. Phys. **121**, 1542 (2004).
[62] B. Xue, J. Wang, and W. Wang, J. Chem. Phys. **119**, 7534 (2003).
[63] C. Chakravarty, J. Chem. Phys. **116**, 8938 (2002).
[64] D. Wright and M. S. El-Shall, J. Chem. Phys. **105**, 11199 (1996).
[65] C. Seko and K. Takatsuka, J. Chem. Phys. **104**, 8613 (1996).
[66] C. Chakravarty, J. Chem. Phys. **102**, 956 (1995).
[67] C. Chakravarty, J. Chem. Phys. **103**, 10663 (1995).
[68] D. J. Wales and R. S. Berry, J. Chem. Phys. **92**, 4283 (1990).
[69] F. Wang and K. D. Jordan, J. Chem. Phys. **119**, 11645 (2003).
[70] B. Hartke, J. Chem. Phys. **97**, 9973 (1993).
[71] Y. Zeiri, Phys. Rev. E **51**, R2769 (1995).
[72] D. M. Deaven and K. M. Ho, Phys. Rev. Lett. **240**, 560 (1995).
[73] D. M. Deaven, N. Tit, J. R. Morris, and K. M. Ho, Chem. Phys. Lett. **195**, 256 (1996).
[74] J. A. Niesse and H. R. Mayne, J. Chem. Phys. **105**, 4700 (1996).
[75] E. Curotto, A. Matro, D. L. Freeman, and J. D. Doll, J. Chem. Phys. **108**, 729 (1998).
[76] M. Falcioni and M. W. Deem, J. Chem. Phys. **110**, 1754 (1999).
[77] J. P. Neirotti, F. Calvo, D. L. Freeman, and J. D. Doll, J. Chem. Phys. **112**, 10340 (2000).
[78] F. Calvo, J. P. Neirotti, D. L. Freeman, and J. D. Doll, J. Chem. Phys. **112**, 10350 (2000).
[79] J. P. Neirotti, D. L. Freeman, and J. D. Doll, Phys. Rev. E **62**, 7445 (2000).
[80] D. D. Frantz, J. Chem. Phys. **102**, 3747 (1995).
[81] D. D. Frantz, J. Chem. Phys. **115**, 6136 (2001).
[82] M. R. Ghayal and E. Curotto, J. Chem. Phys. **111**, 5522 (1999).